CrossMark

Effect of surface heterogeneity on phosphorus adsorption onto mineral particles: experiments and modeling

Zhenghui Cui[1] · Hongwei Fang[1] · Lei Huang[1] · Ke Ni[1] · Danny Reible[2]

Abstract

Purpose Adsorptive interaction at the solid-water interface plays an important role in the fate and behavior of phosphorus (P) in rivers and lakes and the resulting eutrophication. This study aims to investigate the contributions of heterogeneous morphology to P adsorption onto mineral particles.

Materials and methods The dominant minerals in Yellow River sediment, quartz, k-feldspar, and calcite are investigated with adsorption experiments and microscopic examinations. Taylor expansion is applied to quantitatively characterize the heterogeneous surface morphology.

Results and discussion The results reveal that locally concave or convex micro-morphology characterized by the second derivative term of the Taylor expansion, F_2, can be related to adsorption capacity due to its effect on surface-charge density and distribution. The distribution of adsorbed P as a function of F_2 was determined for selected particles composed of each of the pure minerals and was fit to a Weibull distribution. Each mineral was characterized by F_{2a}, the weighted average value of F_2, and Weibull distribution factors, and correlated with sorption isotherms. The developed relationships were used to accurately predict adsorption onto individual particles as well as pure mineral samples.

Conclusions Mineral particles have complex surface morphology, which affects the interface P adsorption. Micro-morphological characterization of F_2 and F_{2a} can be used to predict adsorption onto the pure minerals, and this study provides physical basis for predicting adsorption on sediment particles composed of these minerals.

Keywords Heterogeneous morphology · Microscopic examination · Model modification · Phosphorus adsorption

Responsible editor: Ian Foster

✉ Hongwei Fang
  fanghw@tsinghua.edu.cn

[1] State Key Laboratory of Hydro Science and Engineering, Department of Hydraulic Engineering, Tsinghua University, Beijing 100084, China

[2] Department of Civil, Environmental, and Construction Engineering, Texas Tech University, Lubbock, TX 79409-1023, USA

1 Introduction

Water pollution is of significant concern in many rivers and reservoirs due to an excess supply of nutrients and other contaminants. Phosphorus (P) is a key nutrient for phytoplankton growth and production (Schindler 2006) but is also typically the primary limiting factor for eutrophication (Correll 1998; Withers and Jarvie 2008). Sediment particles have a strong affinity for soluble reactive P due to their high specific surface area and reactive sites (Stumm and Morgan 1981; Meybeck 1982; House and Denison 2002), and P is primarily adsorbed and transported by sediment in aquatic systems (Froelich 1988; Withers and Jarvie 2008). The adsorbed P may accumulate at the bed surface with sediment deposition and be released from particles during sediment re-suspension (Pedro et al. 2013; Huang et al. 2015). Thus, the sediment acts as both source and sink of P through the exchange at the water-sediment interface (House and Denison 2002; Jarvie et al. 2005). Understanding P adsorption onto sediment is critical to understanding P transport and availability and therefore algal growth and eutrophication in such systems (Froelich 1988; Withers and Jarvie 2008).

Much attention has been paid to the factors affecting adsorption, including extrinsic factors such as temperature (Rodda et al. 1996), pH (Robertson and Leckie 1997), and ionic strength (Antelo et al. 2005), and intrinsic sediment properties like the mineral composition (Davis et al. 1998; Zhou et al. 2005) and particle-size distribution (Selig 2003; Wang et al. 2006; Tansel and Rafiuddin 2016). For example, it was concluded that sediments containing high proportions of Fe or Al oxide minerals have a particularly high adsorption capacity (Wang et al. 2009). Moreover, Selig (2003) and Wang et al. (2006) found that the adsorption capacity for sediments with a higher proportion of fine sediment tended to be much greater, which is attributed to the different specific surface area and chemical composition of different size fractions (Sharpley et al. 1994; Zhang et al. 2002). The interfacial micro-characteristics have also been investigated by microscopic examinations and may act as significant factors affecting adsorption (Fang et al. 2013; Li et al. 2016). Atomic force microscopy (AFM) has been used to show the non-uniform distribution of surface charge and reactive sites reflecting variations in local micro-morphology on mineral surfaces (Drelich and Yin 2010; Kumar et al. 2016). This will influence the specific affinity and local electrostatic forces, affecting chemical complexation at surface reactive sites (Rudzinski and Everett 2012).

Adsorption is usually described by empirical isotherms (e.g., Langmuir and Freundlich) that can be used to characterize experimental data (McGechan and Lewis 2002; Zhou et al. 2005). Experimental isotherms, however, provide little insight into the adsorption process and do not provide guidance as to how sediment characteristics will change the isotherms. Avnir et al. (1983) and Pfeifer and Avnir (1983) applied fractal geometry to describe particle surface heterogeneity, and experiments were used to connect the heterogeneity to adsorption (Matsushita and Avnir 1989; Mahnke and Mögel 2003). Kanô et al. (2000) and Skopp (2009) developed a Langmuir adsorption isotherm incorporating fractal dimension in the isotherm parameters. The fractal dimension is largely used as a fitting parameter, however, and does not provide much insight into the surface characteristics. Solid surfaces are also never perfectly regular nor totally fractal as concluded by Rudzinski et al. (2001).

Tosun (2012) and Haerifar and Azizian (2014) demonstrated that the Sips model is more applicable for adsorption in real systems with heterogeneous solid surface by fitting experimental equilibrium data, and it shows a similar form with the fractal model. The fractal-like Sips model is presented as

$$\frac{1}{Q_s} = \frac{1}{Q_m k_s} \left(\frac{1}{C_e} \right)^{\gamma} + \frac{1}{Q_m} \tag{1}$$

where Q_s and Q_m represent the amount of solute adsorbed and the maximum adsorption capacity (mg g^{-1}), respectively; C_e is the equilibrium solute concentration (mg L^{-1}); k_s is a parameter related to the heat of adsorption and reaction rate; and γ is a heterogeneity parameter, and its magnitude is believed to relate with the roughness or heterogeneity of the adsorbent surface (Tosun 2012). In practice, the parameters are simply fit to experimental data and are not directly related to the characteristics of the surface.

In our previous work, Fang et al. (2013, 2014) characterized the particle micro-morphology by a Gaussian distribution of surface curvature and measured the distribution of adsorbed P with curvature on a natural sediment surface to derive an adsorption model. Huang et al. (2016) characterized surface morphology by a Fourier analysis and related this to P adsorption capacity. However, sediment is a complex assemblage of various minerals, such as quartz, feldspar, oxide, and clay minerals, and the mineral composition was not considered in the model of Huang et al. (2016). In the Middle Yellow River of China, for example, the measured mineral composition is about 54% quartz, 35% feldspar, and 6% calcite, with the remainder being primarily various clay minerals (kaolinite, montmorillonite, illite and chlorite). Adsorption behavior of the natural sediment has been estimated from pure mineral behavior using an additive component approach (Tang et al. 1982; Davis et al. 1998).

In this study, we aimed to understand the impacts of heterogeneous surface morphology on P adsorption on these pure minerals (quartz, k-feldspar, calcite), which constitute the majority of coarse river sediments and contribute significantly to the sediment adsorption capacity. It is recognized that the remaining trace clay and other minerals may be important to P adsorption in specific river environments but that sorption to these minerals will always be a substantial component of the sorption onto the composite particle in such systems. AFM was used to relate the heterogeneous local morphology of each mineral to the surface-charge distribution. Scanning electron microscopy (SEM) with energy-dispersive X-ray spectroscopy (EDS) is used to obtain the distribution of adsorbed P on the corresponding micro-morphology. The local curvature (specifically convex or concave character) as defined by the second derivative of the surface is used to describe the surface micro-morphology and related to the statistical probability of P adsorption. The micro-morphology is then related to the parameters in the Sips model to provide a direct relationship between mineral morphology and adsorption.

2 Materials and methods

2.1 Sample preparation

The pure minerals were purchased from the National Center for Reference Material (NCRM), then dried and stored for further analysis and experiments. Mineral samples were ultrasonically dispersed for the measurement of particle-size distribution with the Laser Particle Size Analyzer (HORIBA LA-920), and duplicated experiments were carried out with the

average value presented in this study. Nitrogen adsorption/ desorption isotherms were measured using an ASAP 2020M specific surface area and porosity analyzer. The specific surface area and micro-pore volume were calculated according to the Brunauer-Emmett-Teller (BET) equation (Brunauer et al. 1938) and Barrett-Joyner-Halenda (BJH) method (Barrett et al. 1951), respectively. Surface site density N_s is a significant factor for surface adsorption, and various methods have been developed for measurement, such as tritium exchange (James and Parks 1982), acid-base titration (Sigg and Stumm 1981), and crystallographic characterization (Sposito 1984), or optimized to fit experimental adsorption data (Hayes et al. 1991). For the mineral samples in this study, the range of N_s is initially determined with crystallographic characterization, then optimized to fit the experimental data with MINTEQA2 software (the model parameters and results are shown in the Electronic Supplementary Material).

2.2 Equilibrium adsorption experiments

Phosphorus (added as KH_2PO_4) adsorption was measured in 10-g L^{-1} slurries of each of the pure minerals in 0.1 M $NaNO_3$ over a range of P concentrations (0.0, 0.8, 1.0, 2.0, 3.0, 4.0, 5.0, 8.0, 10.0 mg L^{-1}). Batch experiments were performed in an incubator shaker at 20 ± 2 °C with an oscillation rate of 190 rpm for 24 h. Preliminary kinetic experiments showed that equilibrium was achieved within 24 h. This is also in accordance with the equilibrium time suggested in Wang et al. (2006) and Soinne et al. (2014). The pH of the suspension was kept at 6.5 ± 0.5. After adsorption, the dispersions were centrifuged and supernatant solutions were extracted and filtered with 0.45 μm filter paper. The concentrations of P in the filtrate were determined by the ammonium molybdate spectrophotometric method, using an ultraviolet-visible spectrophotometer at a wavelength of 700 nm (Ministry of Environment Protection of China (MEP) 2001). The adsorbed amount was calculated by the change in solution concentration by material balance. All adsorption experiments were performed in duplicate. The dried solid samples after adsorption in 10 mg L^{-1} were kept in dry apparatus for further SEM and EDS microscopy analysis.

2.3 Microscopic examinations

SEM was used to investigate particle surface morphology. The SEM images are gray pictures and reflect the relative roughness height on the surface. The minerals were adhered onto a metal sample plate with double-sided adhesive and then coated with carbon film to enhance conductivity. Surface morphology and element distribution images were acquired with a Merlin field emission scanning electron microscope (FE-SEM) equipped with EDS to show elemental distribution across the surface. Particles were randomly selected for observation under the field of SEM, simultaneously considering the different particle sizes to ensure that the selected particles could cover a wide size range. Here, a total of 100 particles for each mineral were analyzed, with additional amount of particles exerting only little effect on the results. Experiments were completed in the School of Materials Science and Engineering, Tsinghua University.

As an AFM-based technique, an electrical force microscope (EFM) is used to investigate surface-charge properties by testing electrostatic force between the probe and samples. Experiments are conducted by recording the amplitude and phase shift of the oscillating tip, following the procedure detailed in our previous study (Huang et al. 2012). In lift mode, the tip-sample interaction forces are dominated by electrostatic forces and the phase-shift images provide information of variations of the charge density on the local surface (Gotsmann et al. 1999; Hölscher et al. 2001). Positive frequency shifts correspond to repulsive tip-sample interaction force; negative phase shifts imply attractive forces. Experiments were completed with Dimension 3100 Atomic Force Microscope (AFM) in the Department of Physics, Tsinghua University. Multiple samples and 2~3 different positions in each sample were chosen randomly to enhance the representativeness.

2.4 Surface morphology characterization

Both AFM and SEM can provide information on sediment morphology. AFM can directly provide the surface height while SEM images offer gray values $f(x,y)$ in the form of a matrix. Though gray values are not actual heights, the difference between gray values indicates relative heights on the surface (Fang et al. 2009). Based on these images, the surface height, $f(x,y)$, is expanding in a Taylor series around measurement locations to define the local surface gradient and shape (whether concave or convex as defined by the second derivative).

The surface $f(x,y)$ can be described by a Taylor series about a given point $f(x_a,y_b)$ as

$$f(x,y) = f(x_a + h, y_b + k) = f(x_a,y_b) + \left(h\frac{\partial}{\partial x} + k\frac{\partial}{\partial y}\right)f(x_a,y_b) \quad (2)$$

$$+ \frac{1}{2!}\left(h\frac{\partial}{\partial x} + k\frac{\partial}{\partial y}\right)^2 f(x_a,y_b) + \ldots + \frac{1}{n!}\left(h\frac{\partial}{\partial x} + k\frac{\partial}{\partial y}\right)^n f(x_a,y_b)$$

$$+ \Theta(x_a,y_b),$$

where h and k mean the distance between calculated point $f(x,y)$ and given point $f(x_a,y_b)$ in x and y direction, respectively. $\Theta(x_a,y_b)$ is the Lagrange remainder term.

For simulation of the surface morphology, the value of unknown points $f(x,y)$ in the neighborhood of the dispersed known points $f(x_a,y_b)$ can be calculated with Eq. (3), which is derived from Eq. (2) retaining third-order terms, using the differences between adjacent measurement points.

$$
\begin{aligned}
f(x,y) \approx f(x_a,y_b) &+ \sqrt{hk}\left(c\frac{\Delta f}{\Delta x} + d\frac{\Delta f}{\Delta y}\right) \\
&+ \sqrt{hk}\left[\frac{1}{2!}\left(hc\frac{\Delta^2 f}{\Delta x^2} + 2\sqrt{hk}\frac{\Delta^2 f}{\Delta x\Delta y} + kd\frac{\Delta^2 f}{\Delta y^2}\right)\right] \\
&+ \sqrt{hk}\left[\frac{1}{3!}\left(h^2 c\frac{\Delta^3 f}{\Delta x^3} + 3hkc\frac{\Delta^3 f}{\Delta x^2\Delta y} + 3hkd\frac{\Delta^3 f}{\Delta x\Delta y^2} + k^2 d\frac{\Delta^3 f}{\Delta y^3}\right)\right]
\end{aligned}
\tag{3}
$$

Space intervals are equal, and the dimensionless numbers c and d are defined by $c = \sqrt{h/k}$ and $d = \sqrt{k/h}$. Figure 1 is a schematic diagram for the calculation, and the colored and blank squares represent the known and unknown points on the surface, respectively. Then, the whole surface morphology can be reconstructed with the known point measurements of elevation (Eq. (3)).

The first-order term (F_1) represents the dimensionless height fluctuation in the x and y directions and is defined by Eq. (4).

$$
\begin{aligned}
F_1 = c\frac{\Delta f}{\Delta x} + d\frac{\Delta f}{\Delta y} &= c\frac{f(x_a,y_b)-f(x_{a-1},y_b)}{\Delta x} \\
&+ d\frac{f(x_a,y_b)-f(x_a,y_{b-1})}{\Delta y}
\end{aligned}
\tag{4}
$$

The second-order term (F_2) is defined by Eq. (5)

$$
F_2 = \frac{1}{2!}\left(hc\frac{\Delta^2 f}{\Delta x^2} + 2\sqrt{hk}\frac{\Delta^2 f}{\Delta x\Delta y} + kd\frac{\Delta^2 f}{\Delta y^2}\right)
\tag{5}
$$

$$
\begin{aligned}
&= \frac{hc}{\Delta x}\frac{f(x_{a+1},y_b) + f(x_{a-1},y_b)-2f(x_a,y_b)}{2\Delta x} \\
&+ \frac{\sqrt{hk}}{\Delta x}\frac{f(x_a,y_b) + f(x_{a-1},y_{b-1})-2f(x_{a-1},y_b)}{2\Delta y} \\
&+ \frac{\sqrt{hk}}{\Delta y}\frac{f(x_a,y_b) + f(x_{a-1},y_{b-1})-2f(x_a,y_{b-1})}{2\Delta x} \\
&+ \frac{kd}{\Delta y}\frac{f(x_a,y_{b+1}) + f(x_a,y_{b-1})-2f(x_a,y_b)}{2\Delta y}
\end{aligned}
$$

Based on the equation, F_2 is the dimensionless surface area of an approximate rectangular pyramid formed by the surrounding points. F_2 also represents the curvature of the local morphology, for example, whether the local surface is concave ($F_2 > 0$) or convex ($F_2 < 0$).

The third-order term (F_3) is defined by Eq. (6) and represents the rate of change in curvature.

$$
\begin{aligned}
F_3 &= \frac{1}{3!}\left(h^2 c\frac{\Delta^3 f}{\Delta x^3} + 3hkc\frac{\Delta^3 f}{\Delta x^2\Delta y} + 3hkd\frac{\Delta^3 f}{\Delta x\Delta y^2} + k^2 d\frac{\Delta^3 f}{\Delta y^3}\right)\right] \\
&= \frac{1}{3!}\left\{\frac{h^2 c}{\Delta x^2}\frac{f(x_{a+2},y_b) + 3f(x_a,y_b)-3f(x_{a+1},y_b)-f(x_{a-1},y_b)}{\Delta x}\right. \\
&+ \frac{3hkc}{\Delta x\Delta y}\frac{[f(x_{a+1},y_b) + f(x_{a-1},y_b)-2f(x_a,y_b)]-[f(x_{a+1},y_{b-1}) + f(x_{a-1},y_{b-1})-2f(x_a,y_{b-1})]}{\Delta x} \\
&+ \frac{3hkd}{\Delta x\Delta y}\frac{[f(x_a,y_{b+1}) + f(x_a,y_{b-1})-2f(x_a,y_b)]-[f(x_{a-1},y_{b+1}) + f(x_{a-1},y_{b-1})-2f(x_{a-1},y_b)]}{\Delta y} \\
&+ \left.\frac{k^2 d}{\Delta y^2}\frac{f(x_a,y_{b+2}) + 3f(x_a,y_b)-3f(x_a,y_{b+1})-f(x_a,y_{b-1})}{\Delta y}\right\}
\end{aligned}
\tag{6}
$$

The third-order Taylor expansion can then be written as

$$
f(x,y) \approx f(x_a,y_b) + \sqrt{hk}F_1 + \sqrt{hk}F_2 + \sqrt{hk}F_3,
\tag{7}
$$

where F_1, F_2, and F_3 are local morphology descriptors.

From this calculation, the statistical distribution of F_1, F_2, and F_3 on the particle surface can be obtained, as well as moments of the statistical distribution. In particular, the weighted average morphology F_{ia} of any of the morphological descriptors is calculated by Eq. (8), where K is the fraction of sites within a certain range of values of F_i, corresponding to the distribution of F_i.

$$
F_{ia} = \frac{\sum(|F_i|\cdot K(F_i))}{\sum K(F_i)}
\tag{8}
$$

In this paper, the morphological descriptors (specifically F_2 and F_{2a}, the descriptors related to local concave or convex surface), are related to adsorption onto each of the mineral
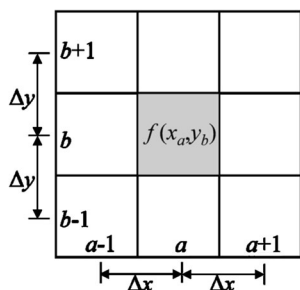
Fig. 1 Schematic diagram of Taylor expansion calculation

surfaces to develop a morphological-based adsorption model based upon the Sips isotherm.

3 Results and discussion

3.1 Mineral properties

Table 1 shows the physicochemical properties of mineral samples used in the experiments. The value of mean size D, specific surface area SSA, micro-pore volume V_m, and total pore volume V_T are obtained directly as summarized in Sect. 2.1. The SSA is a composite parameter that relates with both particle size D and pore volume (V_m or V_T). For the same mineral samples, D shows a considerable effect on SSA, which generally increases with decreasing D; while for different kinds of minerals, distinctive surface micro-lattice structure and cleavage feature, complex micro-morphology, and pore structures on the surface affect the SSA more significantly than the grain size (Walter and Morse 1984; Prikryl et al. 2001). As shown in Table 1, the SSA value increases approximately linearly with increasing V_m or V_T, but not with increasing D. Furthermore, SSA plays an important role in many physical and chemical behaviors (e.g., surface adsorption), especially in characterization of adsorption on complex mineral mixtures or sediment (Prikryl et al. 2001; Yukselen-Aksoy and Kaya 2010). For example, Fontes and Weed (1996) found a fairly good correlation between phosphate adsorption and SSA of the clays with the same size fraction but rather different mineralogy. Huang et al. (2016) compared the estimated P adsorption capacity of two different sediments with similar D_{50} and related the

Table 1 Physicochemical properties of minerals and sediment samples

Sample name	Mean size (D; μm)	Specific surface area (SSA; m^2 g^{-1})	Micro-pore volume (V_m; mm^3 g^{-1})	Total pore volume (V_T; mm^3 g^{-1})	Surface site density (N_s; site nm^{-2})
Quartz	18.07	3.82	2.144	10.52	4.80
K-feldspar	13.71	4.31	2.582	16.36	4.25
Calcite	17.82	1.92	0.936	3.52	5.00

difference to the distinct surface morphology and pore properties. These previous works have also indirectly reflected the impact of heterogeneous surface morphology on adsorption behaviors.

The values of surface site density N_s determined in this study are in accordance with other reported values, e.g., 4.9 ± 1 site nm^{-2} for quartz, 4.05 site nm^{-2} for k-feldspar, and 4.94 site nm^{-2} for calcite (Zhuravlev 1987; Millero et al. 2001; Pokrovsky and Schott 2002; Richter 2015). The mineral species are mainly characterized by N_s, which is determined with the crystalline form and affected by surface defects. For example, quartz consists of SiO_4 tetrahedrons linked together in a three-dimensional framework. The surface defects readily react with water in ambient conditions to form surface reactive sites (=SiOH). Direct measurement from Koretsky et al. (1997) revealed that =SiOH is also the most likely reactive site on k-feldspar ($KAlSi_3O_8$) surface, while =AlOH or =AlOH$_2$ species present in very low concentration. Calcite is a carbonate mineral with a rhombehedral structure; the primary uncharged sites at the surface are =CaOH and =CO$_3$H with 1:1 stoichiometry (Geffroy et al. 1999).

3.2 Heterogeneity of surface-charge distribution

Figure 2 shows the results of AFM with a scanning range of 5.0 μm × 5.0 μm and a storage array of 256 × 256, providing a detailed description of surface morphology and charge distribution. Figure 2a shows the measured surface morphology. Figure 2b is the corresponding phase image obtained under a +5 V bias voltage, where bright regions represent positive phase shift (repulsive electrostatic force between tip and surface), implying positive charges in these regions. The dark regions represent a negative phase shift and negative surface. The existence of both positively and negatively charged regions demonstrate a heterogeneous charge distribution on the quartz surface. Comparing the two figures, it can also be concluded that the complex surface morphology is correlated with charge, as has also been observed with bitumen, volcanic rock, and kaolinite (Drelich and Yin 2010; Kumar et al. 2016).
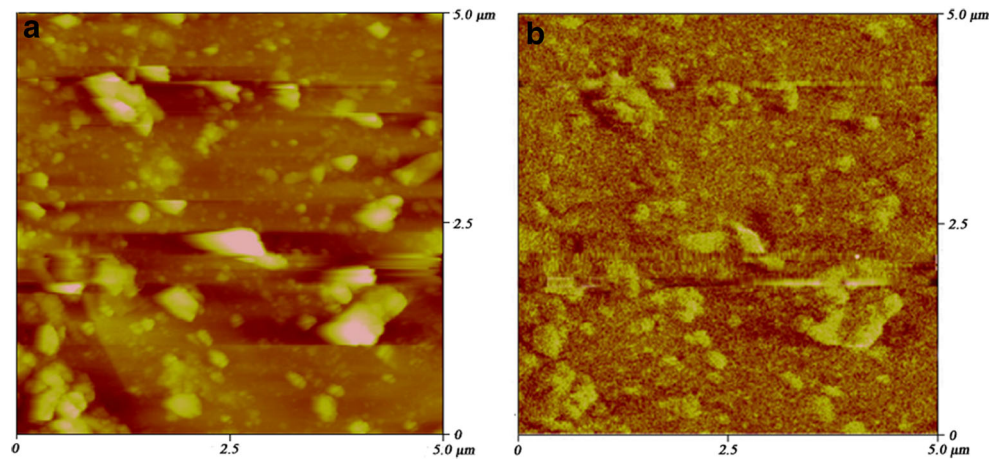
As indicated in Sect. 2.4, we have employed the Taylor expansion to provide a continuous model of the measured particle surface (Eq. (7)). The relationship between the first-, second-, and third-order terms (F_1, F_2, F_3 in Eqs. (4), (5), and (6)) and the phase shift $\Delta\phi$ can be used to relate surface morphology to surface charge (Fig. 3). The x-axis represents morphology descriptors F_1, F_2, and F_3 in Fig. 3a–c, while the y-axis represents the phase shift.

To eliminate the impact of particle size, both the x- and y-axes were normalized as $F_i = F_i/|F_i|_{\max}$, $\Delta\phi_i = \Delta\phi_i/|\Delta\phi_i|_{\max}$. The best correlation between surface charge and morphology was found with the parameter F_2, which suggests that the

Fig. 2 AFM images with quartz sand. **a** Surface morphology. **b** Phase image

curvature of the surface slope dominates surface charge. A fitting equation (Eq. (9)) was developed between F_2 and $\Delta\phi$ and is shown on Fig. 3b.

$$\Delta\phi = 0.337x^3 + 0.481x^2 - 0.932x - 0.045 \qquad (9)$$

F_2 is a descriptor showing whether the local morphology is convex or concave, which appears to have a pronounced effect on charge distribution. Locally convex morphology favors a positive charge, increasing with large $-F_2$ and encouraging phosphate ion adsorption. Locally concave morphology

favors a negative charge, but the charge appears limited at high depth-to-width ratios. Adsorption is likely limited due to steric hindrances at these high depth-to-width ratios.

3.3 Effect of micro-morphology on phosphorus adsorption

The AFM experiments in Sect. 3.2 have shown that F_2 displayed a much better correlation with surface-charge distribution, which influences the local electrostatic force and affects the interfacial adsorption between the charged surface and phosphate ions. In addition, the different derivative terms
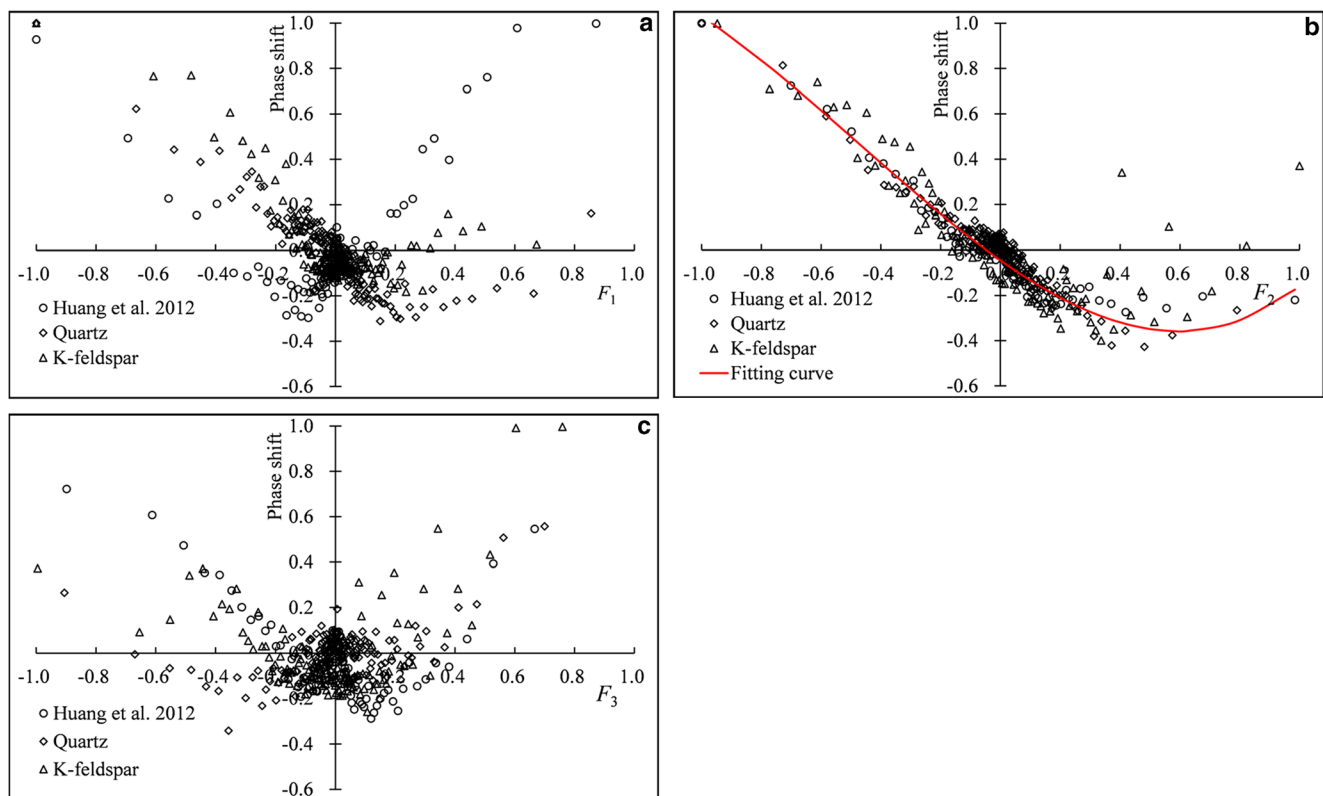

Fig. 3 Relationships between local morphology descriptors and surface-charge distribution. **a** First-order descriptor F_1. **b** Second-order descriptor F_2. **c** Third-order descriptor F_3

F_1, F_2, and F_3 contribute to the particle-surface morphology at different scales, with $F_1 > F_2 > F_3$. Fang et al. (2009, 2014) and Zhang et al. (2013) pointed out that the micro-morphology with a similar scale to the adsorbate would likely play a more significant role in surface adsorption. The quantity $F_2 \cdot \sqrt{hk} = 0.89{\sim}1.44$ (nm), and the average packing area of phosphate, is around 0.6 nm^2 (Goldberg and Sposito 1984), suggesting that this may account for the significance of F_2 in P adsorption.

3.3.1 Phosphorus distribution on particle surface

Distribution maps for specific elements can be determined with EDS. Figure 4 plots the SEM images of original particles and the matching maps of phosphorus distribution before and after adsorption experiments. Different particles for each mineral were selected randomly, with particle size ranges of 10~40 μm for SEM analysis. Black spots in Fig. 4b, d indicate locations where P is adsorbed to the surface.

The comparison in Fig. 4b, d indicates that the pure mineral particles contain little phosphorus on its surface, and adsorbed amounts increase after adsorption experiment.

3.3.2 Adsorption at different surface micro-morphology

The adsorption on individual particles was related to the micro-morphology as indicated by normalized F_2. Figure 5a, b shows the statistical distribution of the total number of measurements of F_2^i, M_i, and number of P adsorbed, N_i, within the interval $\left[F_2^i, F_2^i + \Delta F_2 \right]$ on a single quartz particle.

The ratio of the adsorbed amount to the available surface sites represents an adsorption probability $P_i = N_i / M_i$ within the interval $\left[F_2^i, F_2^i + \Delta F_2 \right]$. Figure 6a, b shows the adsorption probability based on this ratio for quartz and k-feldspar. The adsorption is approximately symmetric at about $F_2 = 0$ (see Fig. 5b) due to the uniform probability of adsorption for $|F_2| < 0.5$, which constitutes the vast majority of the surface.

There is a near-constant probability of adsorption for a surface that exhibits little curvature ($-0.5 < F_2 < 0.5$). Adsorption probability appears to increase for more convex surfaces ($F_2 < -0.5$), where the positive-charge density is high, although the uncertainty is high as well, due to the small number of sites with that morphological characteristic. Adsorption probability decreases for more concave surfaces ($F_2 > 0.5$). This surface morphology has little impact on surface charge (Fig. 3b), but steric hindrances in pores of high depth-to-width ratios likely significantly reduce the adsorption probability.

The analysis of the adsorbed P versus micro-morphology as represented by F_2 was repeated for particles of different size for each of the three minerals. The plots can be normalized by the maximum number of P observed in any micro-morphology, N_m, to remove the influence of the total adsorbed amount in comparing different particles. The measured distribution of N_i / N_m versus $|F_2|$ is depicted in Fig. 7a, b, c for quartz, feldspar, and calcite, respectively. These analyses were repeated

Fig. 4 SEM images of morphology and P distribution on particle surfaces. **a**, **b** SEM and P distribution of quartz before adsorption. **c**, **d** SEM and P distribution after adsorption
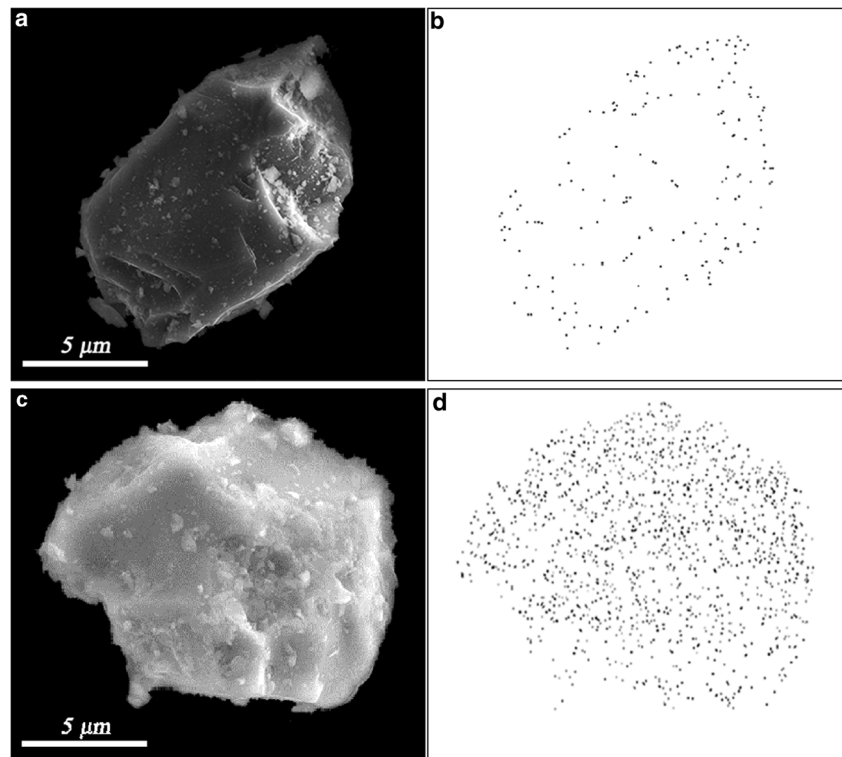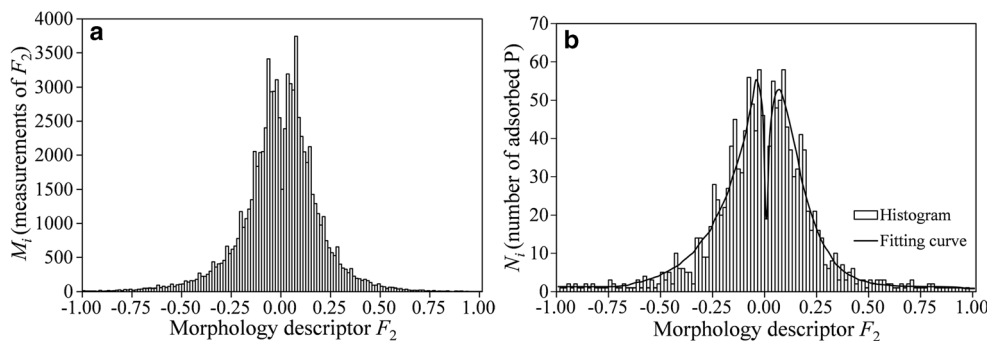
Fig. 5 **a** Number distribution of F_2. **b** Number of absorbed P at different F_2

for different particles of each mineral and the resulting data for normalized sorption as a function of the local magnitude of $|F_2|$ was fit to a Weibull distribution, as shown in Fig. 7.

The distribution of adsorbed P amount at different micro-morphology can be described quantitatively using the three-parameter form of Weilbull function by adjusting two parameters: the shape coefficient, δ, and the scale coefficient, λ, as shown in Eq. (10).
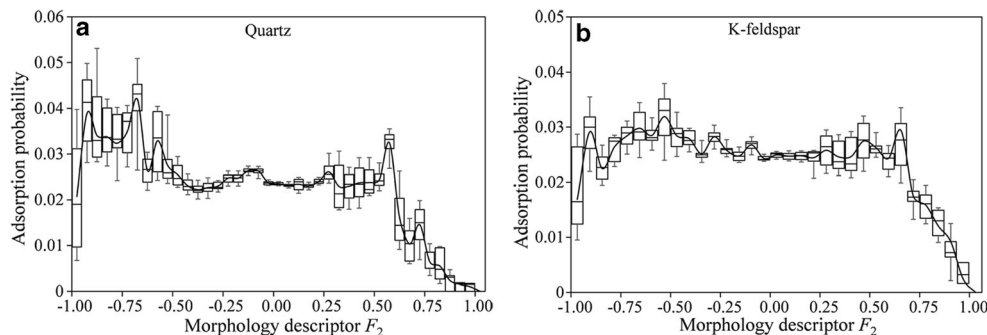
$$W_{(|F_2|,\lambda,\delta)} = \begin{cases} \dfrac{\delta}{\lambda}\left(\dfrac{b|F_2|}{\lambda}\right)^{\delta-1} e^{-(|F_2|/\lambda)^{\delta}} & |F_2| \geq 0 \\ 0 & |F_2| < 0 \end{cases}, (10)$$

where δ ($\delta > 0$) is a coefficient determining the shape of the curve, such as the common exponential and Rayleigh distributions, which are two special cases of Weibull distribution wherein $\delta = 1$ and $\delta = 2$, respectively. λ ($\lambda > 0$) is a coefficient affecting the scale of the curve. $|F_2|$ is the normalized morphology. b means the maximum actual morphology and is a determined value for each individual particle. $W_{(|F_2|,\lambda,\delta)}$ represents the adsorbed amount. The parameters b, δ and λ are presented in Table 2 for each mineral.

3.4 Effect of overall morphology F_{2a} on phosphorus adsorption

Figures 6 and 7 show that P adsorption correlates well with the micro-morphological function $|F_2|$. Thus, the P adsorption on an individual particle should correlate well with the weighted average morphology F_{2a}, which is defined by Eq. (8). The values are shown in Table 2 along with values of individual

Weibull distribution coefficients for the particle. Although the value of F_{2a} as well as the Weibull coefficients may vary on an individual particle, it is expected that a particular mineral will have reproducible average characteristics (Fig. 7), as included in Table 2. These "average" parameters can then be used to predict adsorption on representative samples of each mineral.

3.4.1 Representative accumulated adsorption on single particle

The total adsorption on a particle surface is the accumulation of that adsorbed in a particular micro-morphology and the distribution of the micro-morphology. Considering the apparent symmetry (Fig. 5b) and the Weibull description of P adsorption (Fig. 7), the accumulated adsorption on a particular mineral can be written as

$$A_a^D = 2\int_0^1 W_{(x,\lambda,\delta)}dx = 2\int_0^1 \frac{\delta}{\lambda}\left(\frac{bx}{\lambda}\right)^{\delta-1} e^{-(x/\lambda)^{\delta}}dx, \quad (11)$$

where λ, δ and b are the coefficients of the measured Weibull distribution for that mineral, as shown in Eq. (10). $x = |F_2|$ ($0 \leq x \leq 1$) is the normalized morphology. The integration is over the entire range of $|F_2|$.

3.4.2 Simulation of particle adsorption with the Sips model

The accumulation on the particle can also be expressed as an isotherm. The predicted sorption isotherms on the individual minerals was fit to the fractal-like Sips model (Eq. (1)), and
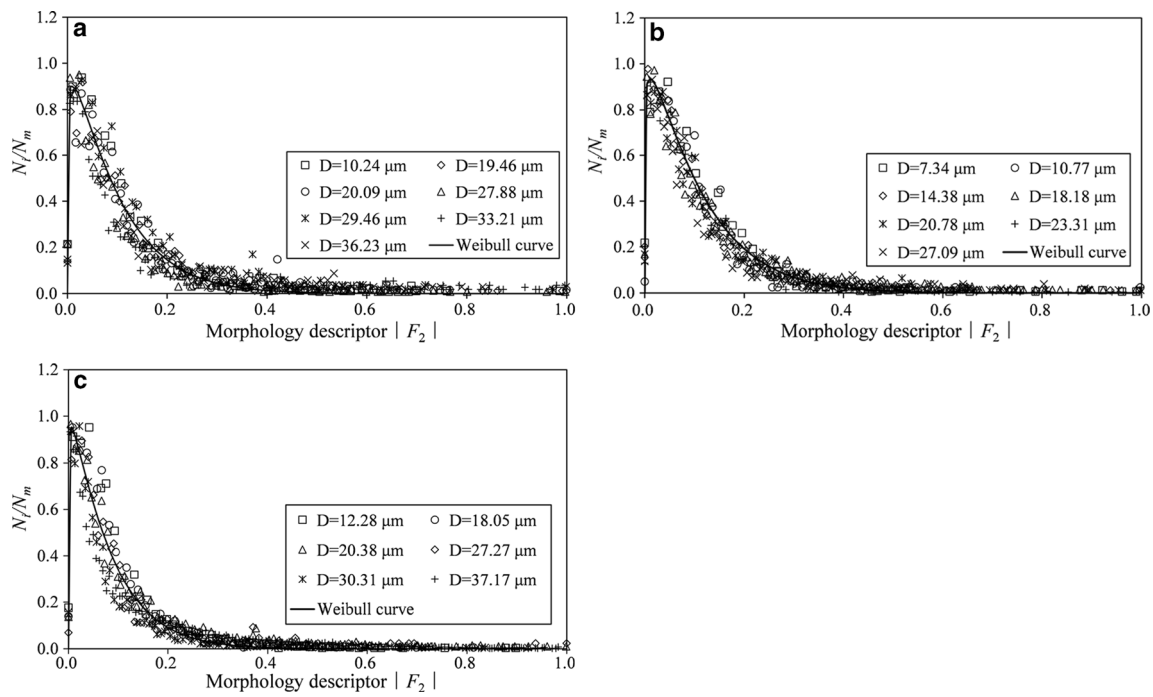
Fig. 6 Heterogeneous adsorption probability on **a** quartz and **b** k-feldspar particle surface

Fig. 7 Statistical relations between adsorbed amount N_i/N_m and local morphology $|F_2|$ with different mineral particles. **a** Quartz. **b** K-feldspar. **c** Calcite

the parameters are shown in Table 3. Figure 8a shows the simulation results of the model.

Table 2 Particle properties and Weibull coefficients

Mineral	D (μm)	F_{2a}	A_a	λ	δ	b
Quartz	10.24	0.135	0.342	0.795	1.201	6.095
	19.46	0.117	0.306	0.986	1.115	6.371
	20.09	0.135	0.348	0.971	1.095	6.181
	27.88	0.100	0.292	0.896	1.063	6.852
	29.46	0.109	0.325	0.918	1.083	6.850
	33.21	0.103	0.272	1.010	1.028	7.818
	36.23	0.098	0.249	1.004	1.030	6.916
Sample	18.07	0.114	0.297	0.940	1.088	6.726
K-feldspar	7.34	0.181	0.315	0.849	1.215	6.454
	10.77	0.179	0.297	0.858	1.178	6.793
	14.38	0.147	0.249	0.840	1.099	7.985
	18.18	0.176	0.323	0.924	1.057	5.882
	20.78	0.162	0.308	0.952	1.063	6.793
	23.31	0.146	0.269	0.862	1.166	8.958
	27.09	0.139	0.241	0.941	1.060	8.372
Sample	13.71	0.161	0.276	0.889	1.120	7.320
Calcite	12.28	0.123	0.315	0.779	1.219	6.333
	18.05	0.106	0.304	0.824	1.145	6.578
	20.38	0.098	0.267	0.953	1.012	7.489
	27.27	0.114	0.305	0.865	1.162	6.540
	30.31	0.108	0.281	0.877	1.086	7.125
	37.17	0.085	0.248	1.071	1.002	8.065
Sample	17.82	0.106	0.285	0.895	1.104	7.022

As all the adsorption experiments are carried out under similar external conditions (temperature, pH, ionic strength, etc.), the differences of the parameters are mainly attributed to the particles' intrinsic properties, such as F_{2a}, D, and N_s. Parameter k_s reflects the reaction rate and is proportional to the ratio between the adsorption and desorption reaction rates. Parameter γ is related to the surface heterogeneity F_{2a}, and larger γ is expected for minerals with greater heterogeneity. By analogy to the work of Kanô et al. (2000), $1/\gamma$ can be viewed as the average number of surface sites covered by one adsorbate molecule, so a larger N_s would suggest a larger $1/\gamma$.

Q_m is the maximum sorption capacity and may be affected by surface heterogeneity, surface area, and the mineral species. The maximum adsorption on each particle Q_m^D (mg g^{-1}) can be calculated by assuming that the adsorption is proportional to adsorption of the minerals that make up the particle (Fang et al. 2014).

$$Q_m^D = \frac{A_a^D}{A_a^S} Q_m \qquad (12)$$

Table 3 Parameters of the Sips model for each mineral sample

Adsorption model	Sample	Quartz	K-feldspar	Calcite
Sips model	Q_m (mg g^{-1})	0.061	0.078	0.106
	k_s	0.292	0.365	0.683
	γ	0.841	0.952	0.762
	R^2	0.987	0.971	0.967

Fig. 8 **a** Fitting results of the Sips adsorption model. **b** Impact of surface heterogeneity F_{2a} on particle adsorption Q_m^D
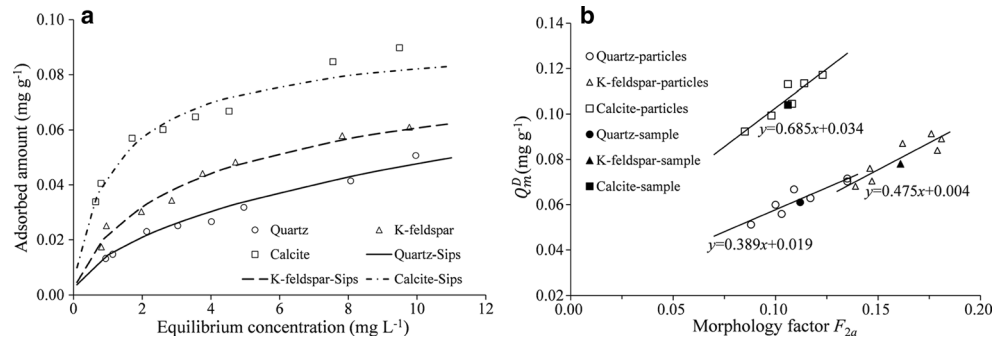
Here, A_a^D and A_a^S are representative total adsorption on an individual particle and mineral sample calculated in Eq. (11). $Q_m(\text{mg g}^{-1})$ is the saturated adsorption of the mineral sample per unit mass (Table 3). Figure 8b shows that the predicted maximum adsorption on an individual particle is related to F_{2a}. For a specific mineral, Q_m^D increases with increasing F_{2a}, and the open symbols represent the predicted sorption as a function of F_{2a} on specific particles.

The relationships were developed with a small number of individual particles. Their ability to represent the mineral was tested by predicting sorption onto the pure mineral mixtures. The results are shown as solid symbols in Fig. 8b. The correspondence between the isotherm generated from the individual particles and the mixture of the pure materials suggests that the isotherms and correlation with F_{2a} provide a good description of the adsorption onto individual minerals.

3.5 Further implications of the findings for pollutant transport models

Pollutant transport models are dependent on both the hydrodynamics and sediment transport due to the adsorption and desorption of contaminants from solids (sediment/mineral particles) (Ji et al. 2002; McGechan and Lewis 2002; Oliveira et al. 2016). Previous models generally either ignore the sediment dynamics or employ simplified empirical partitioning relationships, e.g., a constant distribution coefficient (Sheppard and Thibault 1990; Smits and Van der Molen 1993), or measured non-linear adsorption (Wang et al. 2003; Wool et al. 2006). For example, Wang et al. (2003) developed the P dynamics models with an equation based on Langmuir isotherm to represent the P adsorption by sediment. Some other studies employed surface complexation models in a pollutant transport model (Kent et al. 2000; Curtis et al. 2006). Typically, sediment dynamics are also simplified with sedimentation and erosion coefficients to characterize the deposition and re-suspension of P together with sediment (Chu and Rediske 2011; Huang et al. 2015). P dynamics has also been described with a constant or concentration-related P release rate at the sediment-water interface (Larsen et al. 1979; McDowell and Sharpley 2001). These coefficients and

relations are usually site-specific and not applicable to other systems or conditions.

In this study, particular emphasis was placed on P adsorption mechanism on heterogeneous particle surfaces of different pure minerals in the hope of defining a framework that has broader applicability. These findings presented the effects of surface morphology and mineral properties on P adsorption behavior, such as the micro-distribution (Fig. 7) and the total adsorption amount (Fig. 8), providing physical foundations to improve the P adsorption model, e.g., further modification of the Sips adsorption model with morphology and other intrinsic properties taken into account, or improvement of the surface complexation model by modifying the surface potential-charge relation on heterogeneous particle surface. These improvements would better reflect the effect of sediment properties on P adsorption and are likely to better characterize the P adsorption and transport.

4 Conclusions and prospects

In the present work, we introduce two new factors F_2 and F_{2a} to characterize the surface heterogeneity and relate this to P adsorption. The curvature parameter F_2 characterizes whether the surface is locally concave or convex. The weighted average morphology F_{2a} indicates the average surface heterogeneity or roughness of a particular particle and mineral. Heterogeneous surface charge and adsorption probability is related to F_2. Measurements indicate that the relationship between P adsorption and F_2 is well described by a Weibull distribution function. The overall P adsorption can be correlated with the weighted average value of F_{2a} for a particular surface. The Sips model incorporating the micro-morphology provides a good description of P adsorption.

In this manuscript, P is taken as an example to show the important roles of heterogeneous surface morphology on particle adsorption. The proposed methods can also be applied to the adsorption of other pollutants under varied circumstances, e.g., the heavy metal and radionuclide contamination in coastal and estuary areas (Lee and Cundy 2001; Pan and Wang 2012). More experiments and analyses focusing on the

adsorption of various pollutants on different minerals are necessary to comprehensively understand the impacts of surface heterogeneity on pollutant adsorption and the resultant pollutant transport.

References

Antelo J, Avena M, Fiol S, López R, Arce F (2005) Effects of pH and ionic strength on the adsorption of phosphate and arsenate at the goethite–water interface. J Colloid Interf Sci 285:476–486

Avnir D, Farin D, Pfeifer P (1983) Chemistry in noninteger dimensions between two and three. II. Fractal surfaces of adsorbents. J Chem Phys 79:3566–3571

Barrett EP, Joyner LG, Halenda PP (1951) The determination of pore volume and area distributions in porous substances. I. Computations from nitrogen isotherms. J Am Chem Soc 73:373–380

Brunauer S, Emmett PH, Teller E (1938) Adsorption of gases in multimolecular layers. J Am Chem Soc 60:309–319

Chu X, Rediske R (2011) Modeling metal and sediment transport in a stream-wetland system. J Environ Eng 138:152–163

Correll DL (1998) The role of phosphorus in the eutrophication of receiving waters: a review. J Environ Qual 27:261–266

Curtis GP, Davis JA, Naftz DL (2006) Simulation of reactive transport of uranium (VI) in groundwater with variable chemical conditions. Water Resour Res 42, W04404:1–15

Davis JA, Coston JA, Kent DB, Fuller CC (1998) Application of the surface complexation concept to complex mineral assemblages. Environ Sci Technol 32(19):2820–2828

Drelich J, Yin X (2010) Mapping charge-mosaic surfaces in electrolyte solutions using surface charge microscopy. Appl Surf Sci 256:5381–5387

Fang HW, Chen MH, Chen ZH (2009) Surface characteristics and model of environmental sediment. Science Press, Beijing

Fang HW, Chen MH, Chen ZH, Zhao HM, He GJ (2013) Effects of sediment particle morphology on adsorption of phosphorus elements. Int J Sediment Res 28:246–253

Fang HW, Chen MH, Chen ZH, Zhao HM, He GJ (2014) Simulation of sediment particle surface morphology and element distribution by the concept of mathematical sand. J Hydro-Environ Res 8:186–193

Fontes M, Weed SB (1996) Phosphate adsorption by clays from Brazilian Oxisols: relationships with specific surface area and mineralogy. Geoderma 72:37–51

Froelich PN (1988) Kinetic control of dissolved phosphate in natural rivers and estuaries: a primer on the phosphate buffer mechanism. Limnol Oceanogr 33:649–668

Geffroy C, Foissy A, Persello J, Cabane B (1999) Surface complexation of calcite by carboxylates in water. J Colloid Interf Sci 211:45–53

Goldberg S, Sposito G (1984) A chemical model of phosphate adsorption by soils: I. Reference oxide minerals. Soil Sci Soc Am J 48:772–778

Gotsmann B, Seidel C, Anczykowski B, Fuchs H (1999) Conservative and dissipative tip-sample interaction forces probed with dynamic AFM. Phys Rev B 60:11051

Haerifar M, Azizian S (2014) Fractal-like kinetics for adsorption on heterogeneous solid surfaces. J Phys Chem C 118:1129–1134

Hayes KF, Redden G, Ela W, Leckie JO (1991) Surface complexation models: an evaluation of model parameter estimation using FITEQL and oxide mineral titration data. J Colloid Interf Sci 142:448–469

Hölscher H, Gotsmann B, Allers W, Schwarz UD, Fuchs H, Wiesendanger R (2001) Measurement of conservative and dissipative tip-sample interaction forces with a dynamic force microscope using the frequency modulation technique. Phys Rev B 64:75402

House WA, Denison FH (2002) Exchange of inorganic phosphate between river waters and bed-sediments. Environ Sci Technol 36:4295–4301

Huang L, Fang HW, Chen MH (2012) Experiment on surface charge distribution of fine sediment. Sci China Ser E 55:1146–1152

Huang L, Fang HW, Reible D (2015) Mathematical model for interactions and transport of phosphorus and sediment in the Three Gorges Reservoir. Water Res 85:393–403

Huang L, Fang HW, He GJ, Chen MH (2016) Phosphorus adsorption on natural sediments with different pH incorporating surface morphology characterization. Environ Sci Pollut Res 23:1–9

James RO, Parks GA (1982) Characterization of aqueous colloids by their electrical double-layer and intrinsic surface chemical properties. In: Surface and colloid science. Springer, pp 119–216

Jarvie HP, Jürgens MD, Williams RJ, Neal C, Davies JJ, Barrett C, White J (2005) Role of river bed sediments as sources and sinks of phosphorus across two major eutrophic UK river basins: the Hampshire Avon and Herefordshire Wye. J Hydrol 304:51–74

Ji Z, Hamrick JH, Pagenkopf J (2002) Sediment and metals modeling in shallow river. J Environ Eng 128:105–119

Kanô F, Abe I, Kamaya H, Ueda I (2000) Fractal model for adsorption on activated carbon surfaces: Langmuir and Freundlich adsorption. Surf Sci 467:131–138

Kent DB, Abrams RH, Davis JA, Coston JA, LeBlanc DR (2000) Modeling the influence of variable pH on the transport of zinc in a contaminated aquifer using semiempirical surface complexation models. Water Resour Res 36:3411–3425

Koretsky CM, Sverjensky DA, Salisbury JW, D'Aria DM (1997) Detection of surface hydroxyl species on quartz, γ-alumina, and feldspars using diffuse reflectance infrared spectroscopy. Geochim Cosmochim Ac 61:2193–2210

Kumar N, Zhao C, Klaassen A, Ende DVD, Mugele F, Siretanu I (2016) Characterization of the surface charge distribution on kaolinite particles using high resolution atomic force microscopy. Geochim Cosmochim Ac 175:100–112

Larsen DP, Van Sickle J, Malueg KW, Smith PD (1979) The effect of wastewater phosphorus removal on Shagawa Lake, Minnesota: phosphorus supplies, lake phosphorus and chlorophyll a. Water res 13:1259–1272

Lee SV, Cundy AB (2001) Heavy metal contamination and mixing processes in sediments from the Humber Estuary, Eastern England. Estuar Coast Shelf 53:619–636

Li D, Li Y, Wang Z, Wang X, Li Y (2016) Quantitative, SEM-based shape analysis of sediment particles in the Yellow River. Int J Sediment Res 31:341–350

Mahnke M, Mögel HJ (2003) Fractal analysis of physical adsorption on material surfaces. Colloid Surf A-Physicochem Eng Asp 216:215–228

Matsushita M, Avnir D (1989) The fractal approach to heterogeneous chemistry: surfaces, colloids, polymers. Academic Press, New York

McDowell RW, Sharpley AN (2001) Approximating phosphorus release from soils to surface runoff and subsurface drainage. J Environ Qual 30:508–520

McGechan MB, Lewis DR (2002) Soil and water: sorption of phosphorus by soil, part 1: principles, equations and models. Biosyst Eng 82:1–24

Meybeck M (1982) Carbon, nitrogen, and phosphorus transport by world rivers. Am J Sci 282:401–450

Millero F, Huang F, Zhu X, Liu X, Zhang J (2001) Adsorption and desorption of phosphate on calcite and aragonite in seawater. Aquat Geochem 7:33–56

Ministry of Environment Protection of China (MEP) (2001) Water quality–determination of total phosphorus ammonium molybdate–spectrophotometric method. Natl. Stand. of China, China Standard Press, Beijing

Oliveira DC, Lafon JM, de Oliveira LM (2016) Distribution of trace metals and Pb isotopes in bottom sediments of the Murucupi River, North Brazil. Int J Sediment Res 31:226–236

Pan K, Wang W (2012) Trace metal contamination in estuarine and coastal environments in China. Sci Total Environ 421:3–16

Pedro T, Kimberley S, Fernando P (2013) Dynamics of phosphorus in sediments of a naturally acidic lake. Int J Sediment Res 28:90–102

Pfeifer P, Avnir D (1983) Chemistry in noninteger dimensions between two and three. I. Fractal theory of heterogeneous surfaces. J Chem Phys 79:3558–3565

Pokrovsky OS, Schott J (2002) Surface chemistry and dissolution kinetics of divalent metal carbonates. Environ Sci Technol 36:426–432

Prikryl JD, Jain A, Turner DR, Pabalan RT (2001) Uranium VI sorption behavior on silicate mineral mixtures. J Contam Hydrol 47:241–253

Richter C (2015) Sorption of environmentally relevant radionuclides (U(VI), Np(V)) and lanthanides (Nd(III)) on feldspar and mica. Dissertation, Dresden University of Technology, Dresden

Robertson AP, Leckie JO (1997) Cation binding predictions of surface complexation models: effects of pH, ionic strength, cation loading, surface complex, and model fit. J Colloid Interf Sci 188:444–472

Rodda DP, Johnson BB, Wells JD (1996) Modeling the effect of temperature on adsorption of lead (II) and zinc (II) onto goethite at constant pH. J Colloid Interf Sci 184:365–377

Rudzinski W, Everett DH (2012) Adsorption of gases on heterogeneous surfaces. Academic Press, New York

Rudzinski W, Lee S, Yan CS, Panczyk T (2001) A fractal approach to adsorption on heterogeneous solid surfaces. 1. The relationship between geometric and energetic surface heterogeneities. J Phys Chem B 105:10847–10856

Schindler DW (2006) Recent advances in the understanding and management of eutrophication. Limnol Oceanogr 51:356–363

Selig U (2003) Particle size-related phosphate binding and P-release at the sediment–water interface in a shallow German lake. Hydrobiologia 492:107–118

Sharpley AN, Chapra SC, Wedepohl R, Sims JT, Daniel TC, Reddy KR (1994) Managing agricultural phosphorus for protection of surface waters: issues and options. J Environ Qual 23:437–451

Sheppard MI, Thibault DH (1990) Default soil solid/liquid partition coefficients, KdS, for four major soil types: a compendium. Health Phys 59:471–482

Sigg L, Stumm W (1981) The interaction of anions and weak acids with the hydrous goethite (α-FeOOH) surface. Colloid Surface 2:101–117

Skopp J (2009) Derivation of the Freundlich adsorption isotherm from kinetics. J Chem Educ 86:1341

Smits J, Van der Molen DT (1993) Application of SWITCH, a model for sediment-water exchange of nutrients, to Lake Veluwe in The Netherlands. Hydrobiologia 253:281–300

Soinne H, Hovi J, Tammeorg P, Turtola E (2014) Effect of biochar on phosphorus sorption and clay soil aggregate stability. Geoderma 219:162–167

Sposito G (1984) The surface chemistry of soils. Oxford University Press

Stumm W, Morgan JJ (1981) Aquatic chemistry: chemical equilibria and rates in natural waters. 126. Wiley

Tang HX, Xue HB, Tian BZ, Dong HR, Lei PJ (1982) Study on multicomponent adsorption model of aquatic sediments with a sequential chemical separation procedure. Acta Sci Circumst 2:279–292

Tansel B, Rafiuddin S (2016) Heavy metal content in relation to particle size and organic content of surficial sediments in Miami River and transport potential. Int J Sediment Res 31:324–329

Tosun O (2012) Ammonium removal from aqueous solutions by clinoptilolite: determination of isotherm and thermodynamic parameters and comparison of kinetics by the double exponential model and conventional kinetic models. Int J Env Res Pub He 9:970–984

Walter LM, Morse JW (1984) Reactive surface area of skeletal carbonates during dissolution: effect of grain size. J Sediment Res 54:1081–1090

Wang H, Appan A, Gulliver JS (2003) Modeling of phosphorus dynamics in aquatic sediments: I-model development. Water Res 37:3928–3938

Wang S, Jin X, Bu Q, Zhou X, Wu F (2006) Effects of particle size, organic matter and ionic strength on the phosphate sorption in different trophic lake sediments. J Hazard Mater 128:95–105

Wang Y, Shen Z, Niu J, Liu R (2009) Adsorption of phosphorus on sediments from the Three-Gorges Reservoir (China) and the relation with sediment compositions. J Hazard Mater 162:92–98

Withers P, Jarvie HP (2008) Delivery and cycling of phosphorus in rivers: a review. Sci Total Environ 400:379–395

Wool TA, Ambrose RB, Martin JL, Comer EA, Tech T (2006) Water quality analysis simulation program (WASP). User's Manual, Version 6

Yukselen-Aksoy Y, Kaya A (2010) Predicting soil swelling behaviour from specific surface area. P I Civil Eng-Geotec 163:229–238

Zhang C, Wang L, Li G, Dong S, Yang J, Wang X (2002) Grain size effect on multi-element concentrations in sediments from the intertidal flats of Bohai Bay, China. Appl Geochem 17:59–68

Zhang L, Yang X, Zhang F et al (2013) Controlling the effective surface area and pore size distribution of sp2 carbon materials and their impact on the capacitance performance of these materials. J Am Chem Soc 135:5921–5929

Zhou A, Tang H, Wang D (2005) Phosphorus adsorption on natural sediments: modeling and effects of pH and sediment composition. Water Res 39:1245–1254

Zhuravlev LT (1987) Concentration of hydroxyl groups on the surface of amorphous silicas. Langmuir 3:316–318